



# CHORUS

This is the accepted manuscript made available via CHORUS. The article has been published as:

## Optically pumped dynamic nuclear hyperpolarization in $^{13}\text{C}$ -enriched diamond

Anna J. Parker, Keunhong Jeong, Claudia E. Avalos, Birgit J. M. Hausmann, Christophoros C. Vassiliou, Alexander Pines, and Jonathan P. King

Phys. Rev. B **100**, 041203 — Published 30 July 2019

DOI: [10.1103/PhysRevB.100.041203](https://doi.org/10.1103/PhysRevB.100.041203)

# Optically-pumped dynamic nuclear hyperpolarization in $^{13}\text{C}$ enriched diamond

Anna J. Parker, Keunhong Jeong, Claudia E. Avalos, Birgit J. M. Hausmann,  
Christophoros C. Vassiliou, Alexander Pines, and Jonathan P. King

*Department of Chemistry, University of California, Berkeley, California 94720, United States and  
Materials Sciences Division, Lawrence Berkeley National Laboratory, Berkeley, California 94720, United States*

(Dated: June 4, 2018)

We investigate nuclear spin hyperpolarization from optically polarized nitrogen vacancy centers in isotopically enriched diamonds with  $^{13}\text{C}$  concentrations up to 100%.  $^{13}\text{C}$  enrichment leads to a nitrogen vacancy electron spin resonance with complex hyperfine structure and dynamic nuclear polarization enhancement profile. We show that strongly-coupled  $^{13}\text{C}$  spins in the first shell surrounding a nitrogen vacancy center generate resolved hyperfine splittings, but do not act as an intermediary in the transfer of hyperpolarization of bulk nuclear spins. High levels of  $^{13}\text{C}$  enrichment are desirable to increase the efficiency of hyperpolarization for magnetic resonance signal enhancement, imaging contrast agents, and as a platform for quantum sensing and many-body physics.

PACS numbers:

The last decade has witnessed rapid strides in the development of quantum technologies based on atom-like defect centers in solids<sup>1,2</sup>, such as the negatively-charged nitrogen vacancy ( $\text{NV}^-$ ) center<sup>3</sup>. The  $\text{NV}^-$  is a system of six localized electrons in diamond with a total spin of 1, whose properties have drawn attention from various scientific fields. For example, optical initialization of the  $\text{NV}^-$  spin state<sup>4</sup>, long electron spin coherence times exceeding 1 ms<sup>5,6</sup>, and optical spin state readout<sup>7</sup> have made the defect a model platform for quantum information processing<sup>8-10</sup>, simulation<sup>11,12</sup> and metrology<sup>13-15</sup>.

Nearly all of these technologies require knowledge of and capitalization upon the interactions of the  $\text{NV}^-$  center with nearby nuclear spins both in and external to the diamond. Tuning the  $^{13}\text{C}$  concentration by isotopic growth techniques<sup>16</sup> enables a variety of quantum technology schemes. For instance, in the limit of low nuclear concentrations ( $\leq 1\%$ ),  $\text{NV}^-$  - $^{13}\text{C}$  pairs can form quantum registers<sup>17-19</sup> with increased sensing resolution<sup>20,21</sup> and sensitivity<sup>22</sup>. At slightly higher concentrations ( $\sim 10\%$ ), a single  $\text{NV}^-$  center can be coupled to a number of  $^{13}\text{C}$  nuclei to form the node of a quantum information processor, allowing the indirect fast actuation and universal quantum control on the nuclear spins via the electronic qubit<sup>23,24</sup>. At high concentrations beyond 50% and approaching 100% where internuclear couplings become significant, hybridized nuclear spin states enable decoherence protected subspaces<sup>25</sup> where classical information can be stored. This also forms a versatile system to study various condensed matter phenomena in the strongly dipolar coupled quantum networks<sup>26</sup>, including notions of quantum transport<sup>27</sup>, localization and criticality<sup>28,29</sup>, and Floquet many-body phases<sup>30-32</sup>.

Additionally, optically-polarized electron spin systems like the  $\text{NV}^-$  or the divacancy defect in silicon carbide<sup>33</sup> provide an exciting opportunity for long-standing Nuclear Magnetic Resonance (NMR) and Magnetic Resonance Imaging (MRI) technologies. While NMR and MRI are indispensable tools to the fields of chemistry, biology, engineering and medicine, their sensitivity relies

on nuclear spin initialization (i.e. polarization), which at best reaches  $10^{-4}$  at room temperature. In stark contrast to the weak magnetization of nuclear spins, optical pumping hyperpolarizes the  $\text{NV}^-$  spin state beyond thermal equilibrium at arbitrary temperature and over a wide range of magnetic fields<sup>34</sup>. As a result, a number of schemes for creating nuclear spin hyperpolarization have been reported in the recent literature based on applying traditional dynamic nuclear polarization (DNP) methods<sup>35</sup> to either single  $\text{NV}^-$  centers<sup>36</sup> or  $\text{NV}^-$  ensembles<sup>37-44</sup>. These schemes propose the use of hyperpolarized  $^{13}\text{C}$  nuclei in diamond for use as MRI contrast agents<sup>45</sup> as well as a platform for polarization transfer to external nuclei<sup>43</sup> for enhanced magnetic resonance signal from arbitrary samples. In these cases, the low natural abundance (1.1%) of  $^{13}\text{C}$  nuclear spins limits the efficiency of hyperpolarization and it is desirable to work with  $^{13}\text{C}$  enriched materials.

Here, we report  $\text{NV}^-$  DNP hyperpolarization of  $^{13}\text{C}$  enriched diamonds. Our methods result in significant  $^{13}\text{C}$  bulk polarizations approaching 0.1% at approximately 0.5 T in a variety of samples, an enhancement of three orders of magnitude over thermal polarization. We show how isotopic enrichment imparts a complex structure to the electron spin resonance spectrum and corresponding DNP spectrum. The DNP spectra lend insight to the mechanism of polarization transfer, illustrating that  $\text{NV}^-$  centers and the first shell of  $^{13}\text{C}$  spins behave as a strongly coupled system that transfers polarization directly to weakly coupled nuclear spins. These findings open the path to their use as efficient external polarizing agents, and for applications in quantum technologies.

In this work we employ continuous-wave (CW) DNP to hyperpolarize  $^{13}\text{C}$  nuclei in a set of single crystal diamonds at a magnetic field of approximately 472 mT with the  $\text{NV}^-$  crystal axis aligned along the magnetic field. A schematic of the DNP pulse sequence is given in Figure 1a. Each experiment begins with a set of  $90^\circ$  pulses, which acts to destroy any residual  $^{13}\text{C}$  polarization. This ensures the same initial nuclear polarization for each ex-

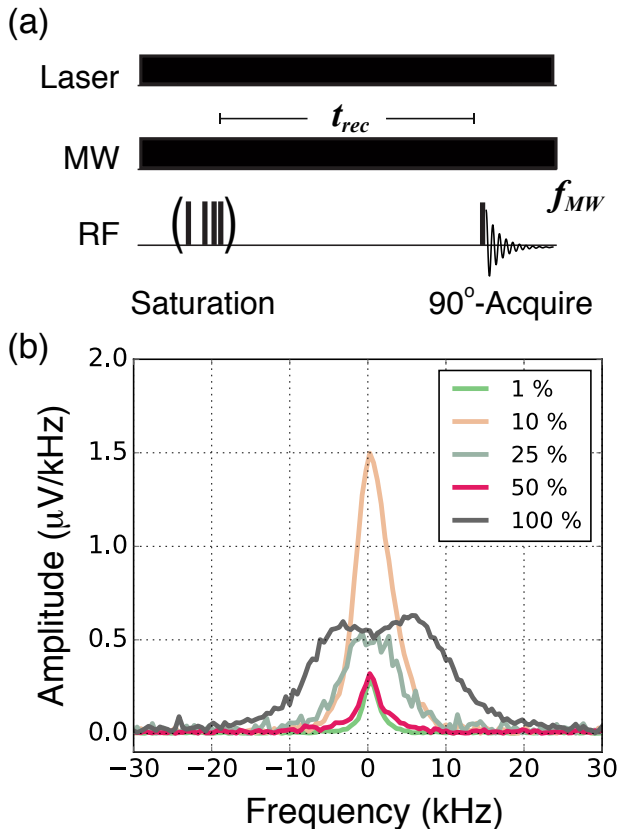


FIG. 1: CW-DNP with  $\text{NV}^-$  centers. A schematic for the CW-DNP experiment is shown in (a). The experiment begins by saturating the spins with a series of  $90^\circ$  pulses, each followed by a dephasing period, which destroys any residual  $^{13}\text{C}$  polarization and ensures the same initial nuclear polarization for each experiment. The  $^{13}\text{C}$  polarization then builds under continuous optical and microwave excitation. The microwave frequency  $f_{MW}$  is swept to find the optimum frequency. After the  $^{13}\text{C}$  nuclear polarization builds during a recovery time  $t_{rec}$ , a single  $90^\circ$  pulse is applied and the NMR signal is acquired. The spectra of the hyperpolarized  $^{13}\text{C}$  NMR resulting from optimizing  $f_{MW}$  and the polarization buildup time are shown in (b) for samples with a natural abundance (1.1%)  $^{13}\text{C}$  and 10, 25, 50, and 100%  $^{13}\text{C}$  enrichment.

periment. The  $^{13}\text{C}$  polarization then builds under continuous optical and microwave irradiation for a recovery time  $t_{rec}$ . The laser optically pumps the  $\text{NV}^-$  center to continually initialize its spin state, while microwave irradiation has the effect of transferring spin polarization between  $\text{NV}^-$  and  $^{13}\text{C}$  spins, thus hyperpolarizing the  $^{13}\text{C}$  spins and producing enhanced NMR signals. The hyperpolarized  $^{13}\text{C}$  NMR spectra of each sample are shown in Figure 1b, where the effects of the nuclear dipole-dipole couplings are apparent in the doublet spectrum of the 100%  $^{13}\text{C}$  diamond.

In a field of 472 mT,  $\text{NV}^-$  spin transitions are observed at approximately 16.1 GHz and 10.3 GHz (Fig. 2a). In this work we focus on the higher-frequency tran-

sition. We read out the  $\text{NV}^-$  spin state via optically-detected magnetic resonance (ODMR), where the  $\text{NV}^-$  fluorescence intensity is monitored while sweeping the microwave frequency. Because the  $m_s = \pm 1$  states are more likely to relax via intersystem crossing to the ground electronic state, resonant microwave excitation produces a detectable change in the  $\text{NV}^-$  fluorescence intensity<sup>3</sup>.  $^{13}\text{C}$  spins within the first shell of nuclei, those directly adjacent to the  $\text{NV}^-$  defect, are strongly coupled to the  $\text{NV}^-$  spin and give a resolved hyperfine structure (Fig. 2). In a  $^{13}\text{C}$  enriched sample, the three nearest-neighbor sites are occupied by 0, 1, 2, or 3  $^{13}\text{C}$  nuclei with the balance occupied by spinless  $^{12}\text{C}$ . The ODMR spectrum is therefore a superposition of 4 distinct patterns of hyperfine splittings with relative intensities determined by the degree of enrichment. The pattern of hyperfine splittings in Fig. 2 is consistent with the known  $^{13}\text{C}$ - $\text{NV}^-$  hyperfine tensor for first-shell nuclear spins<sup>47</sup>.

The DNP process involves driving  $\text{NV}^-$  spin transitions to transfer polarization to nearby  $^{13}\text{C}$  spins. The microscopic mechanism of DNP depends on the degree of homogeneous and inhomogeneous broadening of the electron spin resonance as well as its width relative to the nuclear Larmor frequency  $\omega_n$ <sup>35</sup>. In our experiments the differential solid effect, cross effect, and thermal mixing mechanisms of DNP all potentially contribute, and are difficult to distinguish. In the natural abundance sample the EPR linewidth is likely dominated by strain broadening and interactions with P1 centers, while for the enriched samples hyperfine coupling to  $^{13}\text{C}$  dominates. While the solid effect mechanism is the simplest case involving a single electron and single nuclear spin, cross effect and thermal mixing mechanisms involve two- or multi-electron spin flips whose net energy is on the order of  $\omega_n$ . Cross effect mechanisms tend to dominate in the limit of an inhomogeneously-broadened electron spin resonance while thermal mixing dominates in the limit of a homogeneously broadened electron spin resonance<sup>35,48</sup>. Because our sample composition also varies in  $\text{NV}^-$ , P1 center, and  $^{13}\text{C}$  concentration, it is likely the mechanism varies by sample.

Regardless of the local DNP mechanism, nuclear spin diffusion transports polarization to bulk  $^{13}\text{C}$  spins that do not interact directly with the  $\text{NV}^-$  center. The nuclear spin diffusion constant  $D$  for  $^{13}\text{C}$  in diamond with a natural isotopic abundance is known to be  $6.7 \times 10^{-15} \text{ cm}^2/\text{s}$ <sup>49</sup>. We estimate  $D$  for the other samples using the following relation<sup>50</sup>:

$$D = \frac{\Delta\nu_{dd}a^2}{30} \quad (1)$$

Here,  $\Delta\nu_{dd}$  is the linewidth due to nuclear dipole-dipole coupling, and  $a$  is the average separation between nuclear spins which may be estimated from concentration  $\rho$  by  $a = \rho^{-1/3}$ . Estimating  $\Delta\nu_{dd}$  is straightforward only for the 100%  $^{13}\text{C}$  sample, where the NMR linewidth is clearly dominated by nuclear dipole-dipole interactions

rather than high concentrations of electron spins or magnetic field inhomogeneity, as may be the case for the other samples (see Figure 1). As a result we estimate  $\Delta\nu_{dd}$  from the 100%  $^{13}\text{C}$  sample from the square root of the second moment of the NMR lineshape ( $8.26 \text{ kHz} \pm 0.09$ ). The spin diffusion coefficient typically exhibits a square root dependence on concentration of nuclei for concentrations between 10 and 100%<sup>50,51</sup>, and we use this relationship to estimate  $D$  for the remaining enriched samples. The estimates are given in Table I along with estimates of the spin diffusion length  $L$  during polarization buildup time, calculated with the relation  $L = \sqrt{DT_{DNP}}$ .

In general, the DNP intensity has an antisymmetric frequency dependence and is related to the intensity of the ODMR spectrum (Fig. 3), consistent with DNP mechanisms where the EPR spectrum is broader than the nuclear Larmor frequency. Interestingly, this trend holds for the satellite peaks induced by the strongly hyperfine-coupled  $^{13}\text{C}$  spins in the first shell, indicating that direct driving of the strongly-coupled hyperfine transition does not generate bulk polarization. This contrasts with  $\text{NV}^-$  hyperpolarization near a level anti-crossing where highly mixed electron-nuclear spin states result in hyperpolarization of first-shell  $^{13}\text{C}$  which is then transported to bulk nuclear spins<sup>38</sup>. Here, the symmetric intensities of the hyperfine-induced DNP satellites and the derivative DNP patterns at each satellite transition indicate the polarization of the first-shell  $^{13}\text{C}$  spins does not play a role in the bulk DNP, other than to induce a splitting of the  $\text{NV}^-$  spectrum. Note that this does not mean the first shell nuclei are not being polarized as well, as they are not observed in our experiments.

The level of maximum hyperpolarization is sample dependent due to the varied concentration of  $^{13}\text{C}$ ,  $\text{NV}^-$  centers, and other paramagnetic defects that cause nuclear spin relaxation, see Table I. We note that  $^{13}\text{C}$  enrichment may increase the rate of relaxation alongside increasing the polarization buildup rate, and in fact these rates may be closely linked. The steady-state polarization represents a balance of these processes<sup>52</sup>. The highest level of polarization was achieved in the natural abundance diamond, which has the highest  $\text{NV}^-$  concentration while the highest total magnetization occurred in the 100% diamond. We note that the maximum enhancement observed in the natural abundance sample (1264) is less than reported previously<sup>43</sup>. This may be due to a different sample with different defect concentrations and relaxation times, as well as a different experimental apparatus that may deliver microwave power less efficiently. We regard the present results as being more reliable because of the use of the diamond thermal signal itself as a calibration rather than an external standard<sup>53</sup>. The 100%  $^{13}\text{C}$  diamond also exhibited the fastest buildup of hyperpolarization (Fig. 4), suggesting that the enhanced rate of nuclear spin diffusion more efficiently transports polarization to bulk nuclei. All other parameters being equal, we expect 100%  $^{13}\text{C}$  diamonds to be optimum for MRI contrast and polarization transfer applications. We have

shown that, despite the spectral complexity associated with multiple strong hyperfine couplings, hyperpolarization can be efficiently transferred to bulk nuclear spins. Furthermore, the control we demonstrate over bulk nuclear spin polarization in samples with a high nuclear spin concentration provide insight for and enable development of quantum technologies employing strongly-coupled spin systems.

### Acknowledgement

This work was supported by the U.S. Department of Energy, Office of Science, Basic Energy Sciences under Contract No. DE-AC02-05CH11231. The authors thank Dr. Ashok Ajoy for helpful discussions and Dr. Melanie Drake and Prof. Jeffrey Reimer for providing the natural abundance sample. This study was made possible by the help of Joseph Tabelaing at Applied Diamond Inc./Delaware Diamond Knives for the custom synthesis of the samples used in this study.

### I. MATERIALS AND METHODS

$^{13}\text{C}$  enriched diamonds were grown by chemical vapor deposition (Applied Diamond Inc.) using  $^{13}\text{C}$  enrichments of methane with 600 ppm nitrogen as a precursor.  $^{13}\text{C}$  concentrations of 10%, 25%, 50%, and 100%  $^{13}\text{C}$  were used. These samples were compared to a sample grown by high-pressure high-temperature (HPHT) diamond synthesis (Sumitomo Electric Industries, Inc.) with a substitutional nitrogen concentration of approximately 200 ppm and  $^{13}\text{C}$  concentration of 1.1% (natural abundance). All samples were irradiated with 1 MeV electrons at a fluence of  $10^{18} \text{ cm}^{-2}$  (Prism Gem LLC) and annealed at  $800^\circ\text{C}$  for 2 h to produce an  $\text{NV}^-$  concentration of 1-10 ppm. Optically detected magnetic resonance (ODMR) and DNP were performed in a purpose-built instrument consisting of a custom probe fixed in an electromagnet (GMW Associates, Model 3472-50 with Danfysik 858 power supply). The probe includes a radiofrequency circuit for inductive NMR excitation and detection, a goniometer for two-axis alignment of the defect axis along the magnetic field, a 3 mm wire loop for microwave excitation (Agilent E8257D signal generator), and optical access to the sample (532 nm Coherent Verdi G5 laser). For all DNP experiments, the amplitude of the microwave frequency was set to 10 dBm and amplified with 3 W amplifier (Mini-Circuits ZVE-3W-183+) before being sent to the 3 mm loop. The NMR circuit includes a 30-turn planar coil of 46 AWG copper wire, with capacitance added to impedance-match the circuit at 5.06 MHz. The NMR component of DNP experiments are carried out with a Magritek Kea<sup>2</sup> console. For ODMR measurements, the microwave amplitude was modulated 100% at 200 Hz from the reference signal of the lock-in amplifier (Stanford Research Systems, SR830) and the

Sample	D1	D2	D3	D4	D5
$[^{13}\text{C}]$ (%)	1	10	25	50	100
$\Delta\nu_{NV}$ (MHz)	17	26	23.5	27	52
$T_{DNP}$ (s)	$22.34 \pm 0.06$	$59.55 \pm 0.03$	$36.14 \pm 0.02$	$42.94 \pm 0.04$	$15.28 \pm 0.02$
Enhancement	$1264 \in [854, 2430]$	$1094 \pm 202$	$318 \pm 22$	$138 \pm 4$	$604 \pm 11$
$P_{enh}$ (%)	$0.10 \in [0.071, 0.20]$	$0.091 \pm 0.017$	$0.026 \pm 0.002$	$0.011 \pm 0.0004$	$0.050 \pm 0.0009$
$\Delta_{DNP}$ (MHz)	14	17	30	20	52
D ( $10^{14}$ cm <sup>2</sup> /s)	0.67	2.06	3.26	4.62	6.53
L (nm)	3.87	11.09	10.86	14.08	9.99

TABLE I: Summary of the polarization buildup time  $T_{DNP}$ , enhanced  $^{13}\text{C}$  nuclear polarization ( $P_{enh}$ ) and maximum DNP enhancement for each diamond sample as well as parameters useful for evaluating DNP mechanisms ( $\Delta\nu_{NV}$ ,  $\Delta_{DNP}$ ), estimates of spin diffusion constants (D) and the spin diffusion length (L) during polarization buildup.

fluorescence signal was detected with an avalanche photodiode (APD 410A, Thorlabs). The lock-in amplifier measured the in-phase component of the fluorescence signal at the modulation frequency using a time constant of 30 ms. A spectrum was acquired by stepping through a range of microwave frequency centered on the  $\text{NV}^-$  ESR, where each step consists of changing the microwave frequency by one step, waiting 50 ms, and measuring the ODMR signal from the lock-in. These spectra were used to characterize the samples, align the defect axis along the magnetic field, and set the strength of the magnetic field as measured by the ensemble of  $\text{NV}^-$  defects for DNP experiments.

DNP experiments were carried out at 472.2 mT. A schematic of the DNP experiment is shown in Figure 1. A 532 nm laser with a beam diameter of approximately 5 mm is set to an output power of 1 W/cm<sup>2</sup> and applied continuously throughout experiments. The laser beam is kept large to irradiate the full surface of the diamond. A set of 90° pulses are used to destroy thermal  $^{13}\text{C}$  polarization before waiting a time  $t_{rec}$  for  $^{13}\text{C}$  polarization to build as a result of DNP processes. The microwave frequency is set to  $f_{MW}$  and applied continuously for the duration of  $t_{rec}$ . A simple 90 pulse-acquire experiment is then used to determine the  $^{13}\text{C}$  NMR signal. This is repeated for a range of  $f_{MW}$  centered on the  $\text{NV}^-$  ESR to acquire the DNP spectrum of  $^{13}\text{C}$  NMR signal as a function of microwave frequency  $f_{MW}$ . The  $^{13}\text{C}$  NMR signal was compared by fitting the free induction decay (FID) at  $f_{MW,i}$  to the FID of the signal with max-

imum enhancement by a scaling factor. All data are reported with error bars giving 95% confidence intervals for the scaling factors, taken from the standard deviation of the parameter estimates of the fit. All NMR raw data were acquired with Prospa (software supplied with the Kea<sup>2</sup> spectrometer) and exported for processing in Python with Matplotlib<sup>55</sup>, SciPy and NumPy<sup>56,57</sup> packages<sup>58</sup>.

Photoluminescence (PL) experiments<sup>59</sup> were carried out with a homebuilt confocal microscope to gain a qualitative understanding of the defect content in each of the samples. The confocal microscope involves a 532 nm laser (Opto Engine LLC, MGL-III-532-200mW) directed to the sample through a microscope objective with NA = 0.4 (Nikon M Plan 20 ELWD). From this NA we estimate an excitation volume of  $1.9 \times 10^5 \mu\text{m}^3$ . The objective is also used to collect the fluorescence and direct it through a dichroic mirror to a spectrometer (Mightex HRS-BD1-025). The emission of the samples were collected using an approximate optical excitation power of 2.5 kW/cm<sup>2</sup>. We use the minimum optical power required to detect the emission spectra with the Mightex Spectrometer in order to suppress any changes in the emission spectra due to charge-state conversion between  $\text{NV}^-$  and  $\text{NV}^0$ . Emission spectra were collected from sixteen random points in each of the samples. Each spectrum was averaged 256 times with an exposure time of 100 ms. The raw data were acquired using the software provided by Mightex for interfacing with the spectrometer, and exported for processing in Python.

<sup>1</sup> W. F. Koehl, B. B. Buckley, F. J. Heremans, G. Calusine, and D. D. Awschalom, *Nature* **479**, 84 (2011).

<sup>2</sup> M. Widmann, S.-Y. Lee, T. Rendler, N. T. Son, H. Fedder, S. Paik, L.-P. Yang, N. Zhao, S. Yang, I. Booker, et al., *Nature Materials* **14**, 164 (2015).

<sup>3</sup> M. W. Doherty, N. B. Manson, P. Delaney, F. Jelezko, J. Wrachtrup, and L. C. L. Hollenberg, *Physics Reports* **528**, 1 (2013), ISSN 03701573, arXiv:1302.3288v1, URL <http://dx.doi.org/10.1016/j.physrep.2013.02.001>.

<sup>4</sup> N. Manson and R. McMurtrie, *Journal of Luminescence* **127**, 98 (2007), proceedings of the Ninth International

Meeting on Hole Burning, Single Molecule, and Related Spectroscopies: Science and Applications, Hole Burning, Single Molecule, and Related Spectroscopies: Science and Applications, URL <http://www.sciencedirect.com/science/article/B6TJH-4N56BY8-4/2/fe207946349634f71860c2b4ad4ebf3a>.

<sup>5</sup> G. Balasubramanian, P. Neumann, D. Twitchen, M. Markham, R. Kolesov, N. Mizuochi, J. Isoya, J. Achard, J. Beck, J. Tissler, et al., *Nat Mater* **8**, 383 (2009).

<sup>6</sup> D. J. Christle, A. L. Falk, P. Andrich, P. V. Klimov, J. U. Hassan, N. T. Son, E. Jánzén, T. Ohshima, and D. D.

- Awschalom, *Nature Materials* **14** (2015).
- 7 M. W. Doherty, N. B. Manson, P. Delaney, and L. C. L. Hollenberg, *New Journal of Physics* **13**, 025019 (2011), URL <http://stacks.iop.org/1367-2630/13/i=2/a=025019>.
  - 8 N. Yao, L. Jiang, A. Gorshkov, P. Maurer, G. Giedke, J. Cirac, and M. Lukin, *Nat Commun* **3**, 800 (2012), URL <http://dx.doi.org/10.1038/ncomms1788>.
  - 9 B. Hensen, H. Bernien, A. E. Dréau, A. Reiserer, N. Kalb, M. S. Blok, J. Ruitenber, R. F. Vermeulen, R. N. Schouten, C. Abellán, et al., *Nature* **526**, 682 (2015).
  - 10 P. V. Klimov, A. L. Falk, D. J. Christle, V. V. Dobrovitski, and D. D. Awschalom, *Science advances* **1**, e1501015 (2015).
  - 11 J. Cai, A. Retzker, F. Jelezko, and M. B. Plenio, *Nature Physics* **9**, 168 (2013).
  - 12 A. Ajoy and P. Cappellaro, *Phys. Rev. Lett.* **110**, 220503 (2013), URL <http://link.aps.org/doi/10.1103/PhysRevLett.110.220503>.
  - 13 J. M. Taylor, P. Cappellaro, L. Childress, L. Jiang, D. Budker, P. R. Hemmer, A. Yacoby, R. Walsworth, and M. D. Lukin, *Nature Phys.* **4**, 810 (2008).
  - 14 J. R. Maze, P. L. Stanwix, J. S. Hodges, S. Hong, J. M. Taylor, P. Cappellaro, L. Jiang, A. Zibrov, A. Yacoby, R. Walsworth, et al., *Nature* **455**, 644 (2008).
  - 15 G. Balasubramanian, I.-Y. Chan, R. Kolesov, M. Al-Hmoud, C. Shin, C. Kim, A. Wojcik, P. R. Hemmer, A. Krüger, F. Jelezko, et al., *Nature* **445**, 648 (2008).
  - 16 N. Bar-Gill, L. Pham, C. Belthangady, D. Le Sage, P. Cappellaro, J. Maze, M. Lukin, A. Yacoby, and R. Walsworth, *Nat. Commun.* **3**, 858 (2012), URL <http://dx.doi.org/10.1038/ncomms1856>.
  - 17 M. V. G. Dutt, L. Childress, L. Jiang, E. Togan, J. Maze, F. Jelezko, A. S. Zibrov, P. R. Hemmer, and M. D. Lukin, *Science* **316**, 1312 (2007).
  - 18 P. Neumann, R. Kolesov, B. Naydenov, J. Beck, F. Rempp, M. Steiner, V. Jacques, G. Balasubramanian, M. L. Markham, D. J. Twitchen, et al., *Nat Phys* **6**, 249 (2010).
  - 19 A. Reiserer, N. Kalb, M. S. Blok, K. J. van Bemmel, T. H. Tamini, R. Hanson, D. J. Twitchen, and M. Markham, *Physical Review X* **6**, 021040 (2016).
  - 20 A. Laraoui, F. Dolde, C. Burk, F. Reinhard, J. Wrachtrup, and C. A. Meriles, *Nature communications* **4**, 1651 (2013).
  - 21 T. Roskopf, J. Zopes, J. Boss, and C. Degen, *arXiv preprint arXiv:1610.03253* (2016).
  - 22 A. Ajoy, Y. Liu, and P. Cappellaro, *arXiv preprint arXiv:1611.04691* (2016).
  - 23 N. Khaneja, *Phys. Rev. A* **76**, 032326 (2007).
  - 24 T. W. Borneman, C. E. Granade, and D. G. Cory, *Phys. Rev. Lett.* **108**, 140502 (2012), URL <http://link.aps.org/doi/10.1103/PhysRevLett.108.140502>.
  - 25 N. Kalb, A. A. Reiserer, P. C. Humphreys, J. J. Bakermans, S. J. Kamerling, N. H. Nickerson, S. C. Benjamin, D. J. Twitchen, M. Markham, and R. Hanson, *Science* **356**, 928 (2017).
  - 26 H. Weimer, N. Y. Yao, and M. D. Lukin, *Physical review letters* **110**, 067601 (2013).
  - 27 A. Ajoy and P. Cappellaro, *Phys. Rev. B* **87**, 064303 (2013), URL <http://link.aps.org/doi/10.1103/PhysRevB.87.064303>.
  - 28 N. Y. Yao, C. R. Laumann, S. Gopalakrishnan, M. Knap, M. Mueller, E. A. Demler, and M. D. Lukin, *Physical review letters* **113**, 243002 (2014).
  - 29 R. Nandkishore and D. A. Huse, *Annu. Rev. Condens. Matter Phys.* **6**, 15 (2015).
  - 30 V. Khemani, A. Lazarides, R. Moessner, and S. L. Sondhi, *Physical review letters* **116**, 250401 (2016).
  - 31 D. V. Else and C. Nayak, *Physical Review B* **93**, 201103 (2016).
  - 32 S. Choi, J. Choi, R. Landig, G. Kucsko, H. Zhou, J. Isoya, F. Jelezko, S. Onoda, H. Sumiya, V. Khemani, et al., *Nature* **543**, 221 (2017).
  - 33 A. L. Falk, P. V. Klimov, V. Ivády, K. Szász, D. J. Christle, W. F. Koehl, Á. Gali, and D. D. Awschalom, *Physical review letters* **114**, 247603 (2015).
  - 34 E. Scott, M. Drake, and J. A. Reimer, *Journal of Magnetic Resonance* **264**, 154 (2016).
  - 35 T. Wenckeback, *Essentials of Dynamic Nuclear Polarization* (Spindrift, Burgh-Haamstede, The Netherlands, 2016), ISBN 978907.
  - 36 P. London, J. Scheuer, J.-M. Cai, I. Schwarz, A. Retzker, M. Plenio, M. Katagiri, T. Teraji, S. Koizumi, J. Isoya, et al., *Physical review letters* **111**, 067601 (2013).
  - 37 R. Fischer, A. Jarmola, P. Kehayias, and D. Budker, *Physical Review B - Condensed Matter and Materials Physics* **87**, 1 (2013), ISSN 10980121, 1202.1072.
  - 38 G. A. Álvarez, C. O. Bretschneider, R. Fischer, P. London, H. Kanda, S. Onoda, J. Isoya, D. Gershoni, and L. Frydman, *Nature Communications* **6**, 8456 (2015), ISSN 2041-1723, 1412.8635, URL <http://www.nature.com/doi/10.1038/ncomms9456>.
  - 39 J. P. King, P. J. Coles, and J. A. Reimer, *Physical Review B - Condensed Matter and Materials Physics* **81**, 1 (2010), ISSN 10980121.
  - 40 J. Scheuer, I. Schwartz, Q. Chen, D. Schulze-Sunninghausen, P. Carl, P. Hofer, A. Retzker, H. Sumiya, J. Isoya, B. Luy, et al., *New Journal of Physics* **18**, 13040 (2016), ISSN 13672630, 1601.05967.
  - 41 Q. Chen, I. Schwarz, F. Jelezko, A. Retzker, and M. B. Plenio, *Physical Review B - Condensed Matter and Materials Physics* **92**, 20 (2015), ISSN 1550235X, 1504.02368.
  - 42 Q. Chen, I. Schwarz, F. Jelezko, A. Retzker, and M. B. Plenio, *Physical Review B - Condensed Matter and Materials Physics* **93**, 1 (2016), ISSN 1550235X, 1510.03256.
  - 43 J. P. King, K. Jeong, C. C. Vassiliou, C. S. Shin, R. H. Page, C. E. Avalos, H.-j. Wang, and A. Pines, *Nature Communications* **6**, 8965 (2015), ISSN 2041-1723, 1501.2897, URL <http://dx.doi.org/10.1038/ncomms9965>.
  - 44 B. L. Green, B. G. Breeze, G. J. Rees, J. V. Hanna, J.-P. Chou, V. Ivády, A. Gali, and M. Newton, *Physical Review B* **96**, 054101 (2017).
  - 45 E. Rej, T. Gaebel, T. Boele, D. E. J. Waddington, and D. J. Reilly, *Nature Communications* **6**, 8459 (2015), ISSN 2041-1723, arXiv:1502.06214v1, URL <http://dx.doi.org/10.1038/ncomms9459>.
  - 46 A. J. Parker, H.-J. Wang, Y. Li, A. Pines, and J. P. King, *Decoherence-protected transitions of nitrogen vacancy centers in 99% <sup>13</sup>C-enriched diamond* (2015), arXiv:1506.05484.
  - 47 J. H. Shim, B. Nowak, I. Niemeyer, J. Zhang, F. D. Brandão, and D. Suter, arXiv:1307.0257 (2013).
  - 48 D. Shimon, Y. Hovav, A. Feintuch, D. Goldfarb, and S. Vega, *Physical Chemistry Chemical Physics* **14**, 5729 (2012).
  - 49 C. J. Terblanche, E. C. Reynhardt, and J. A. van Wyk, *Solid state nuclear magnetic resonance* **20**, 1 (2001).
  - 50 H. Hayashi, T. Itahashi, K. Itoh, L. Vlasenko, and

- M. Vlasenko, *Physical Review B* **80**, 045201 (2009), ISSN 1098-0121, URL <http://link.aps.org/doi/10.1103/PhysRevB.80.045201>.
- <sup>51</sup> C. Kittel and E. Abrahams, *Physical Review* **90**, 238 (1953), ISSN 0031899X.
- <sup>52</sup> See supplemental material at [url will be inserted by publisher] for sample characterization including relaxation times.
- <sup>53</sup> See supplemental material at [url will be inserted by publisher] for a description of the calibration against thermal equilibrium.
- <sup>54</sup> See supplemental material at [url will be inserted by publisher] for a discussion of defect concentration.
- <sup>55</sup> J. D. Hunter, *Computing In Science & Engineering* **9**, 90 (2007).
- <sup>56</sup> S. van der Walt, S. C. Colbert, and G. Varoquaux, *Computing in Science & Engineering* **13**, 22 (2011).
- <sup>57</sup> E. Jones, T. Oliphant, P. Peterson, et al., *SciPy: Open source scientific tools for Python* (2001–), URL "<http://www.scipy.org/>".
- <sup>58</sup> See supplemental material at [url will be inserted by publisher] for further discussion of data analysis.
- <sup>59</sup> See supplemental material at [url will be inserted by publisher] for a description of the photoluminescence experiments.

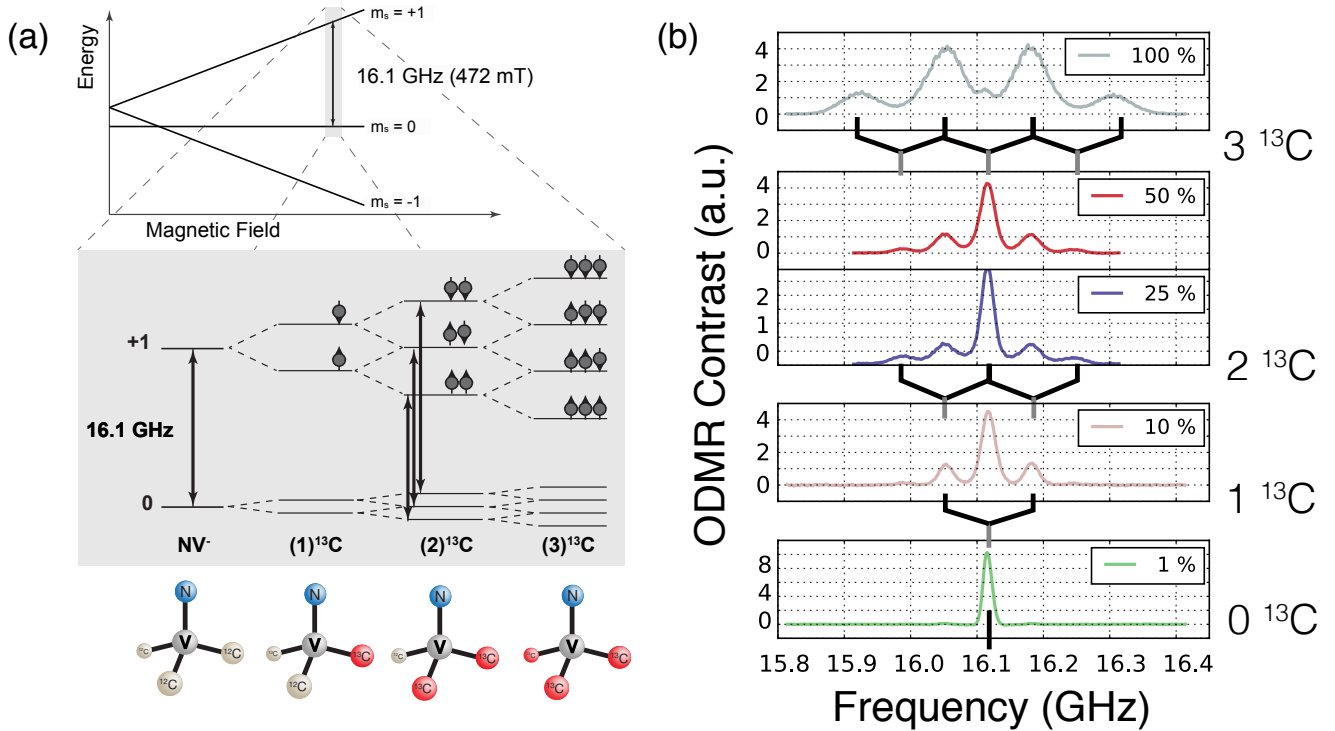


FIG. 2: The effect of <sup>13</sup>C enrichment on the energy level structure and ODMR spectroscopy of NV<sup>-</sup> centers. The energy level structure of the NV<sup>-</sup> as a function of magnetic field strength is shown in (a), where the magnetic field regime relevant to DNP experiments is highlighted and expanded. In this work, we focus on the high energy transition from the NV<sup>-</sup>  $m_s = 0$  to  $m_s = +1$  at 472 mT, which has a frequency of approximately 16.1 GHz. The strongest hyperfine interactions occur between the NV<sup>-</sup> and its first-shell <sup>13</sup>C nuclei, those directly adjacent to it. Occupation of the first-shell sites leads to a splitting in not only the NV<sup>-</sup>  $m_s = \pm 1$  levels, but also the  $m_s = 0$  due to the anisotropic component of the coupling. The magnified energy level diagram shows how the NV<sup>-</sup> spin states split into hyperfine states determined by the different possible combinations of nuclear spin, as 1, 2, and 3 carbons are added. Diagrams of the NV<sup>-</sup> as well as the occupation of the first shell sites with <sup>13</sup>C nuclei are given below the energy level diagram. The branching in these energy levels corresponds directly to the structure seen in the ODMR spectra of diamonds with varying <sup>13</sup>C enrichment (b). A single line is observed for the  $m_s = 0$  to  $m_s = +1$  transition in NV<sup>-</sup> spin state for a sample with a natural abundance (1.1%) of <sup>13</sup>C, whereas a sample with 100% <sup>13</sup>C enrichment exhibits a quartet for the same transition.<sup>46</sup>



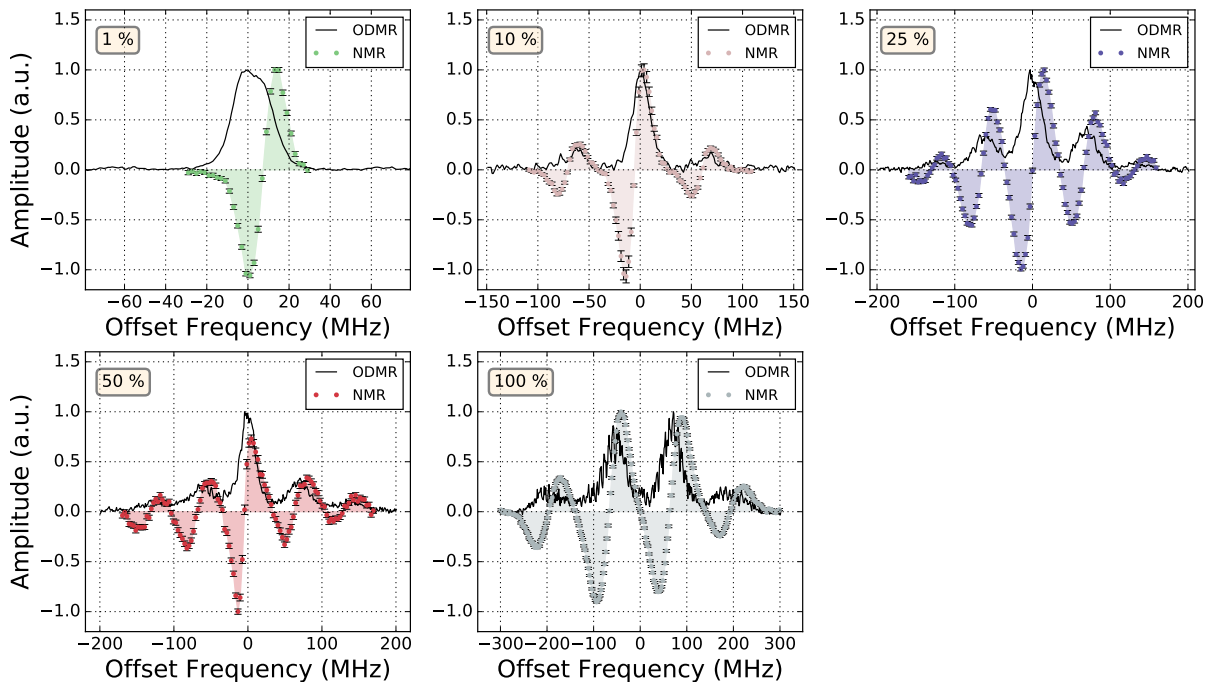


FIG. 3: DNP spectra of the various diamond samples. Normalized hyperpolarized  $^{13}\text{C}$  NMR signal as a function of offset microwave frequency for each sample. The normalized ODMR data for each sample is given to show the corresponding high frequency transition of the  $\text{NV}^-$  ESR spectrum. CW-DNP experiments are performed at 472.1 - 473.0 mT, thus the microwave frequency is centered at approximately 16.1 GHz for the various samples with an  $^{13}\text{C}$  NMR frequency of approximately 5.06 MHz. It should be noted the SNR of the ODMR spectra shown here differs from that of the ODMR spectra in Figure 2 because the two were acquired at different microwave amplitudes. The optimum microwave amplitude for DNP measurements is higher than the microwave amplitude for optimized ODMR contrast (see Materials and Methods).

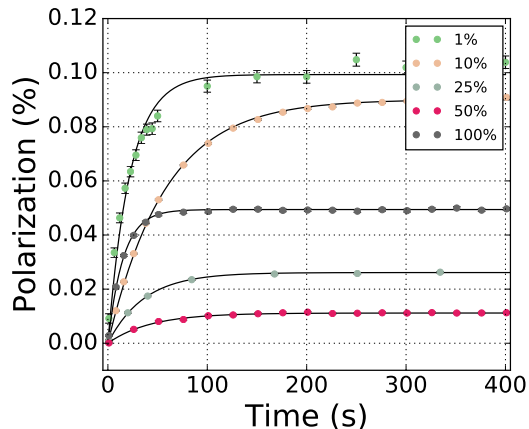


FIG. 4:  $^{13}\text{C}$  polarization buildup curves are summarized for all samples involved in the study. Characteristic polarization buildup times  $T_{DNP}$  are given in Table I. The sample with 100%  $^{13}\text{C}$  enrichment gives the fastest buildup and the largest signal. The maximum polarization as well as the second-fastest buildup rate is observed from the sample with a natural abundance of  $^{13}\text{C}$ , which is likely due to it having the highest concentration of  $\text{NV}^-$  centers<sup>54</sup>.